Complex flow in lowest crustal, anastomosing mylonites: Strain gradients in a Kohistan gabbro, northern Pakistan

Laurent Arbaret, Jean-Pierre Burg

Complex flow in lowest crustal, anastomosing mylonites: Strain gradients in a Kohistan gabbro, northern Pakistan

L. Arbaret[1] and J.-P. Burg

Geologisches Institut, ETH-Zentrum, Zurich, Switzerland

Received 6 November 2002; revised 3 April 2003; accepted 14 May 2003; published 9 October 2003.

[1] Strain localization in near paleo-Moho metagabbros of the Kohistan Arc, northern Pakistan, produced anastomosing shear zones. The two-dimensional (2-D) analysis of strain gradients in planes parallel to the general flow direction reveals simple shear strain >7 combined with about 50% surface loss. The pargasite-garnet assemblage of the mylonite has a density 2.8% higher than the protolith, which is insufficient to account for the measured surface loss. Furthermore, major and trace element compositions of the gabbro and the mylonite indicate isochemical deformation. Average V_p and acoustic impedance measured at room temperature and up to 300 MPa increase from gabbro through the gradient zone to mylonite; they are consistent with density measurements. The three-dimensional analysis of shape-preferred orientation and lattice-preferred orientation of sheared and synkinematic minerals indicates that the 2-D surface loss reflects sideways and lengthwise material transfer. Sideways and lengthwise material transfers take place in widening and lengthening mylonites, respectively. The anastomosing shear zone pattern impels this complexity of the regional flow. We conclude that shear zones with a thinning component are likely representative of deep crustal flow in other tectonic environments. *INDEX TERMS:* 8025 Structural Geology: Mesoscopic fabrics; 8030 Structural Geology: Microstructures; 8099 Structural Geology: General or miscellaneous; *KEYWORDS:* shear zone, lower crust, island arc, Kohistan

Citation: Arbaret, L., and J.-P. Burg, Complex flow in lowest crustal, anastomosing mylonites: Strain gradients in a Kohistan gabbro, northern Pakistan, *J. Geophys. Res.*, *108*(B10), 2467, doi:10.1029/2002JB002295, 2003.

1. Introduction

[2] Strain localization in high-grade rocks results in ductile shear zones. These shear zones typically consist of planar mylonite zones bounded by strain gradients that display continuous transition to the relatively unstrained protolith [e.g., *Ramsay*, 1980]. Across these gradients, finite strain profiles are classically calculated from the reorientation of passive markers such as xenoliths [*Ramsay and Allison*, 1979], dikes [e.g., *Escher et al.*, 1975], or crystalline aggregates [e.g., *Burg and Laurent*, 1978; *Dutruge et al.*, 1995; *Srivastava et al.*, 1995; *Michibayashi et al.*, 1999]. However, strain measurements show mylonites with plane strain, constriction and apparent flattening fabrics, and progressive transition from one type to another during a single progressive shear event [e.g., *Passchier*, 1998; *Ring*, 1999]. These spatial changes in strain geometry may appear in shear zones with irregularly thick mylonites bordered by deforming wall rocks [*Passchier*, 1998]. This complex geometry is illustrated by arrays of shear zones anastomosing around lenses of less deformed rock. The symmetry of the resulting patterns reflects the bulk deformation regime [*Gapais et al.*, 1987], symmetric conjugate shear zones reflect coaxial deformation, and asymmetric shear zone patterns reflect the asymmetry of the regional deformation (e.g., S/C surfaces [*Berthé et al.*, 1979] and Riedel systems [*Riedel*, 1929; *Tchalenko*, 1968]). The aim of this study was to investigate the geometric features of deformed gabbros at the near paleo-Moho crustal sequence of the Kohistan paleo-island arc, with *Means'* [1995, p. 160] premise that "...rocks themselves should be our best guides to rock behaviour". We apply the structural techniques of shear zone studies to elucidate the relative contributions of pure shear, simple shear, and volume changes in these lower crustal rocks. We place emphasis on features suggesting strain partitioning and disturbances of the ideal simple shear flow around relatively stiff lenses. We finally point out the complex nature of variations in the rock fabric.

2. Geological Settings

[3] The Kohistan paleo-island arc, in the western Himalayas, has been described by several authors [e.g., *Tahirkheli et al.*, 1979; *Bard*, 1983; *Coward et al.*, 1986; *Treloar et al.*, 1996]. The plutonic calc-alkaline rocks that form the lowest crustal levels are dominantly sheared gabbros, hornblende-gabbros, and diorites [*Treloar et al.*, 1990; *Burg et al.*, 1998]. In these rocks, a spectacular pattern of anastomosing

[1]Now at Institut des Sciences de la Terre, Université d'Orléans, Orléans, France.

0148-0227/03/2002JB002295$09.00

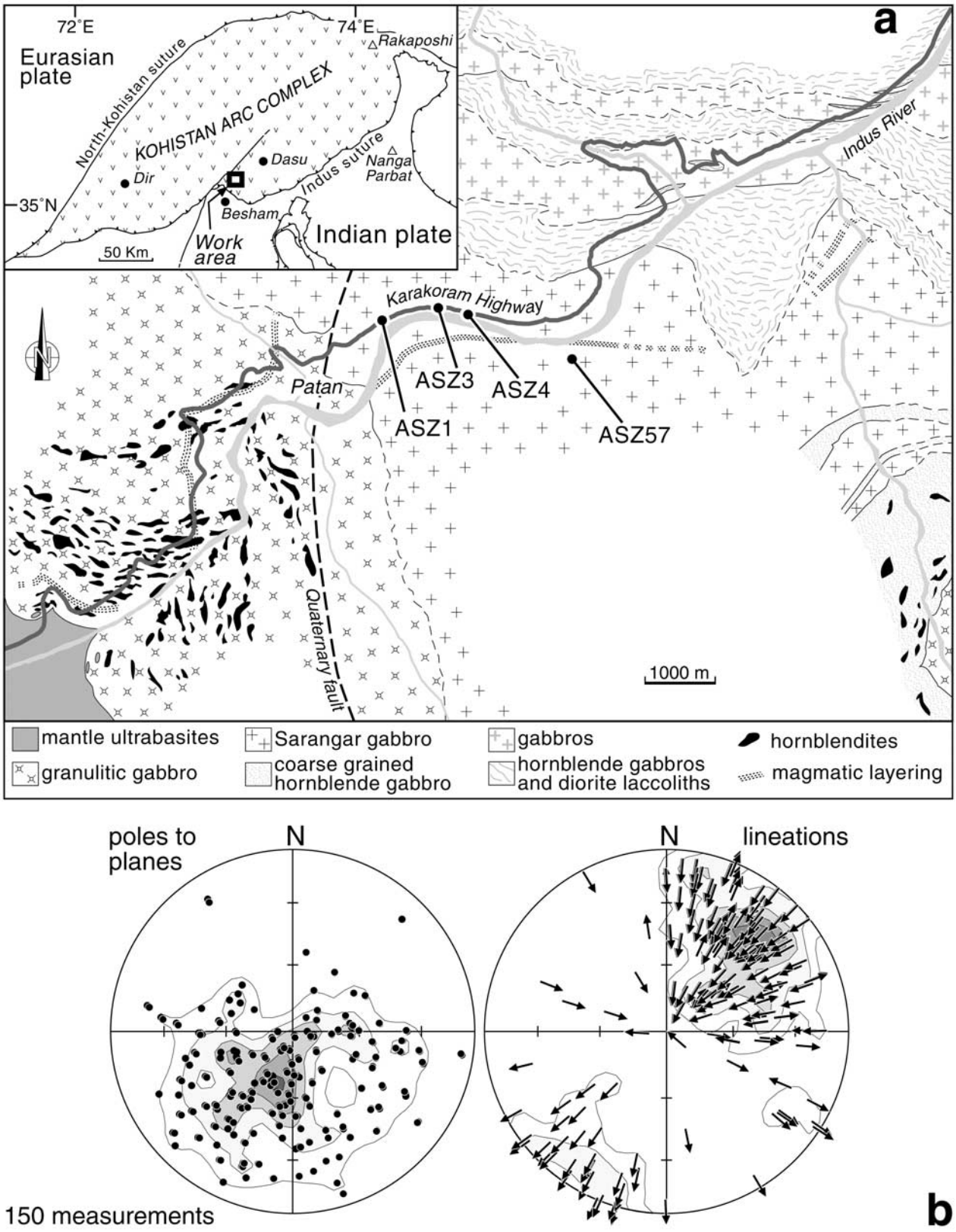

Figure 1. (a) Location of the studied shear zones (geographical coordinates in Table 1). Geological map from the work of *Arbaret et al.* [2000]. (b) Lower hemisphere equal-area projection of poles to planes and stretching lineation of anastomosing shear zones with arrows pointing in the shear direction. Starkey density contours are 2, 4, 6, 8, and 10%.

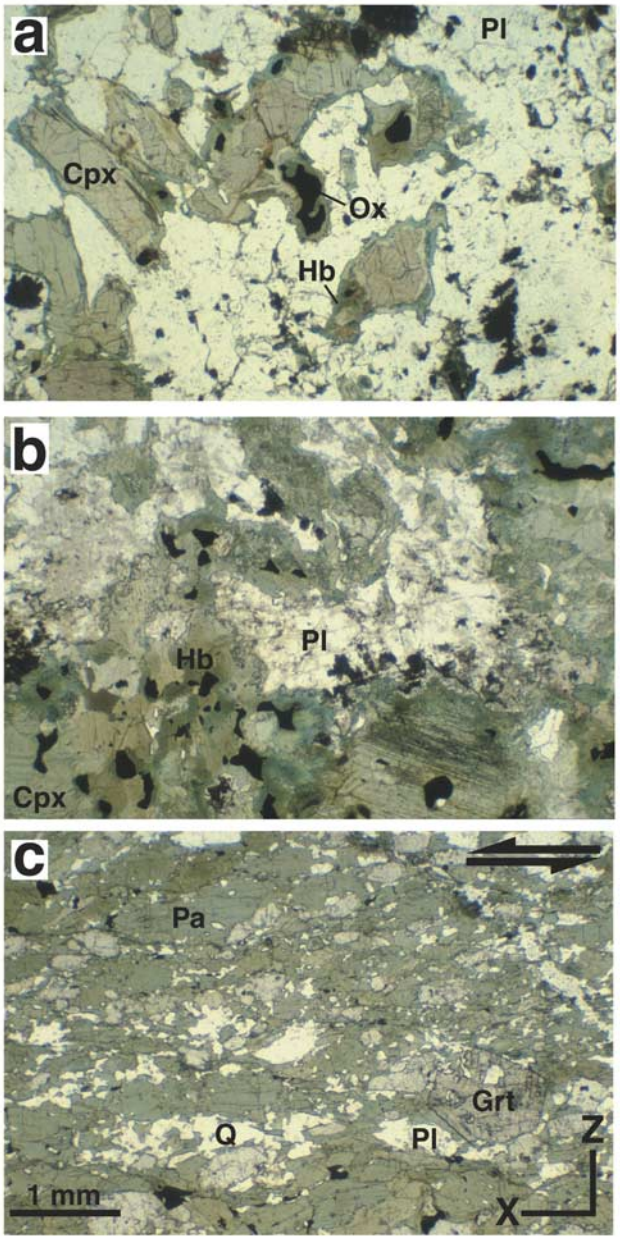

Figure 2. Crossed-polarizer photomicrographs of [*XZ*] thin sections. (a) Protolith, partially recrystallized magmatic assemblage with amphibole coronas around pyroxene and oxides. (b) Low-strain domain, amphibole and plagioclase crystallized at the expense of pyroxene. (c) High-strain mylonite, granoblastic metamorphic assemblage with euhedral garnet (Cpx, clinopyroxene; Grt, garnet; Hb, hornblende; Ox, oxide; Pa, pargasite; Pl, plagioclase; Q, quartz). Scale is the same for Figures 2a–2c.

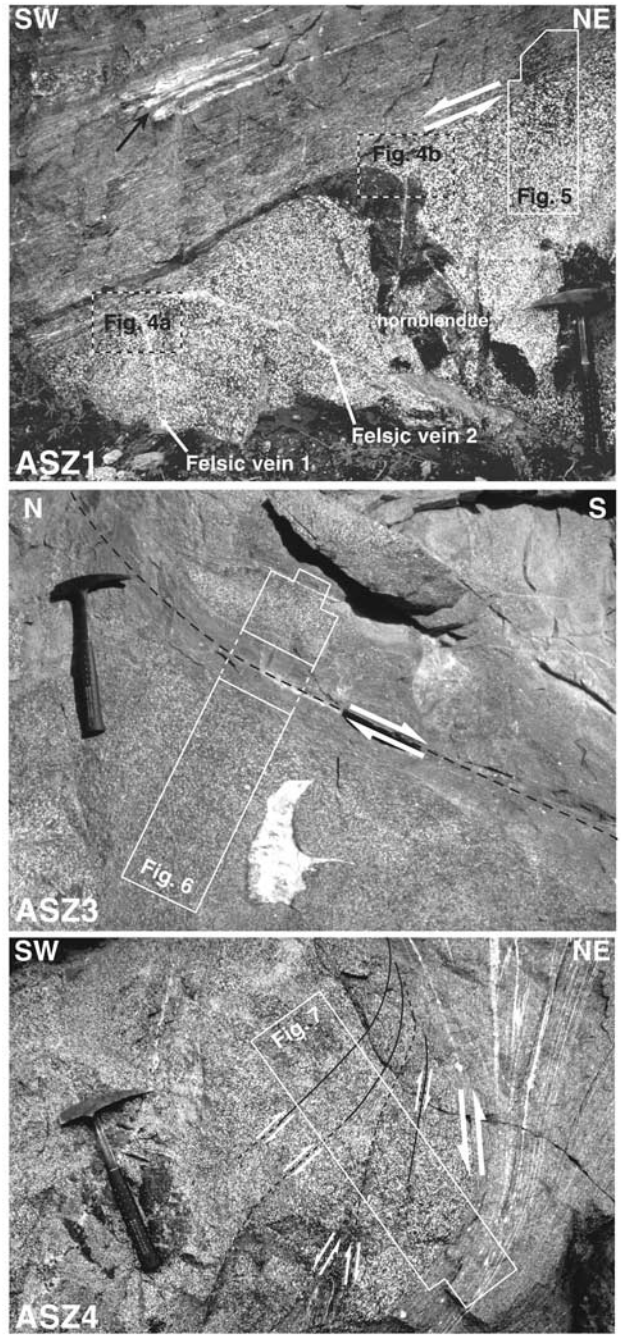

Figure 3. [*XZ*] field views of the studied shear zones. White arrows denote sense of shear. ASZ 1, 15-cm-wide strain gradient in footwall of a shallow-dipping shear zone. A hornblendite vein and two felsic veins are deflected. Black arrow denotes folded felsic vein in the mylonite. ASZ 3, sharp strain gradients between two gabbro lenses. A late quartz pocket (white irregular zone) occupies the central part of the footwall lens. ASZ 4, progressively curved and thinned (bottom right) mylonite. Small antithetic shear bands (underlined with black lines) are strain accommodation features imposed at the gabbro lens boundaries.

shear zones developed during distributed, southwest vergent noncoaxial deformation in the mantle-crust transition zone of the time [*Arbaret et al.*, 2000]. Typically, strain gradients include progressively curved rock foliations, whose strain ratio increases toward mylonites, which are fine-grained and dark amphibolites with few feldspar porphyroclasts. The study focused on shear zones in the so-called Sarangar gabbro (Figure 1a). This gabbro comprises a coarse-grained,

Table 1. GPS Geographical Coordinates, Structural Data, Field Image Properties, and Analysis Procedure of the Studied ASZ Shear Zones

	ASZ			
	1	3	4	57
GPS				
Longitude	73.01221°E	73.01862°E	73.02483°E	73.03110°E
Latitude	35.11730°N	35.12019°N	35.12050°N	35.11603°N
Protolith				
Foliation (strike/dip), deg	165/83 SW	56/69 NW	75/72 S	72/84 S
Lineation (direction/plunge), deg	125/76 NW	37/9 SW	102/34 E	73/5 E
Shear zone				
Foliation (strike/dip), deg	116/20 S	14/43 E	28/14 NW	105/18 S
Lineation (direction/plunge), deg	30/19 SW	8/6 S	38/8 SW	15/18 S
Sense of shear	top to SW	top to South	top to SW	top to South
Original image				
Size, pixels	12921 × 9333	12750 × 3000	11500 × 2750	1450 × 942
Scale, pixels/cm	200	200	200	99
Orientation (strike/dip), deg	30/90	2/48 W	41/76 SE	15/90
Image analysis				
Size of images, pixels	500 × 500	500 × 500	500 × 500	290 × 290
Step of grid, pixels	250 × 250	250 × 250	250 × 250	145 × 145
Number of images	130	230	221	109

garnet-free assemblage of hypidioblastic orthopyroxene, clinopyroxene, plagioclase, amphibole, epidote, and accessory quartz [*Yoshino et al.*, 1998] (Figure 2a). From protolith to mylonite, the magmatic assemblage evolves through the progressive development of ferroan-pargasitic to tchermakitic amphibole rims around diopside (Figure 2b). In mylonites, the stable metamorphic assemblage is composed of fine-grained pargasitic to tchermakitic amphiboles, epidote, plagioclase, quartz, and poikiloblastic garnet [*Zeilinger*, 2002] (Figure 2c). Partial melting generated

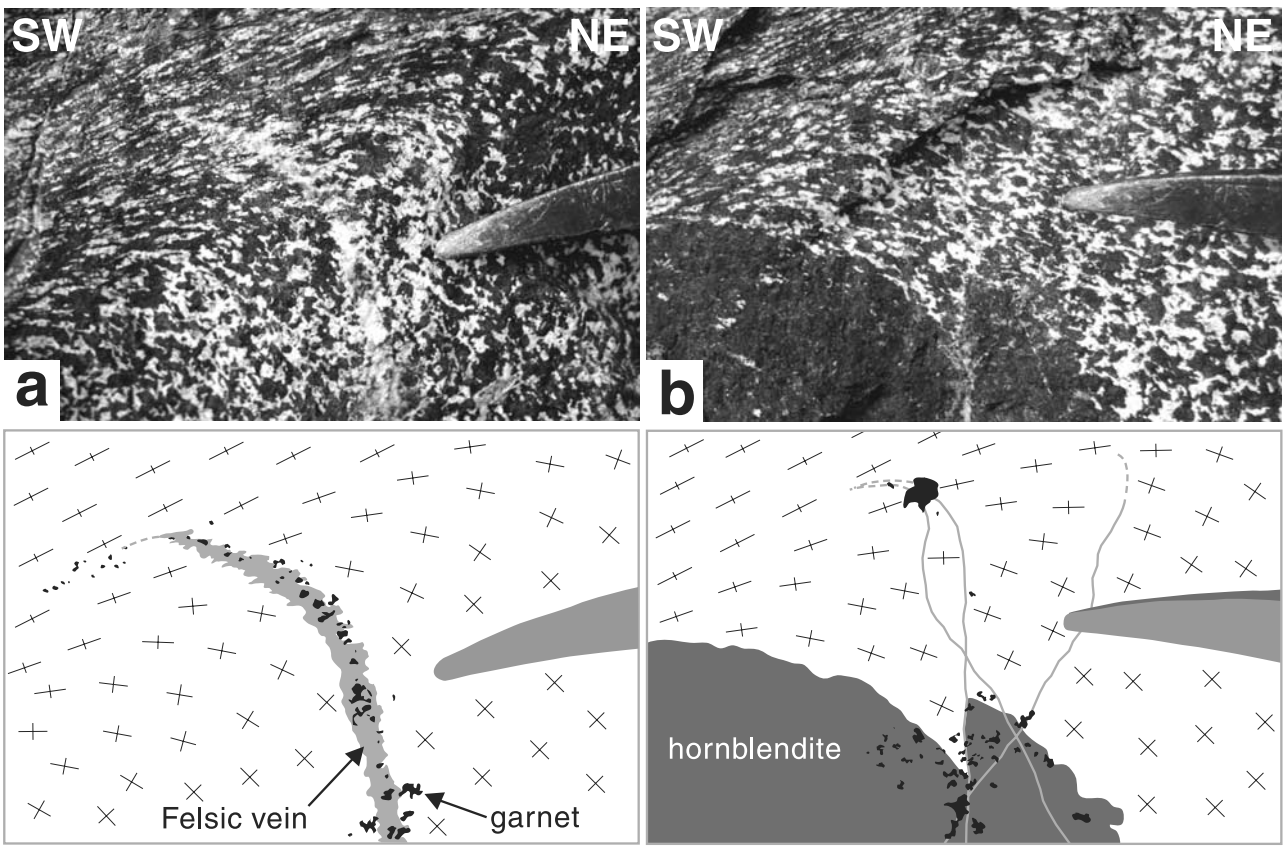

Figure 4. ASZ 1 shear zone. Crosscutting relationships between deflected felsic veins and the bent foliation of (a) the country gabbro and (b) the hornblendite. Note the reactional garnet (sketches) bordering the veins and particularly developed near the contact between veins and hornblendite. [*XZ*] sections, locations as in Figure 3.

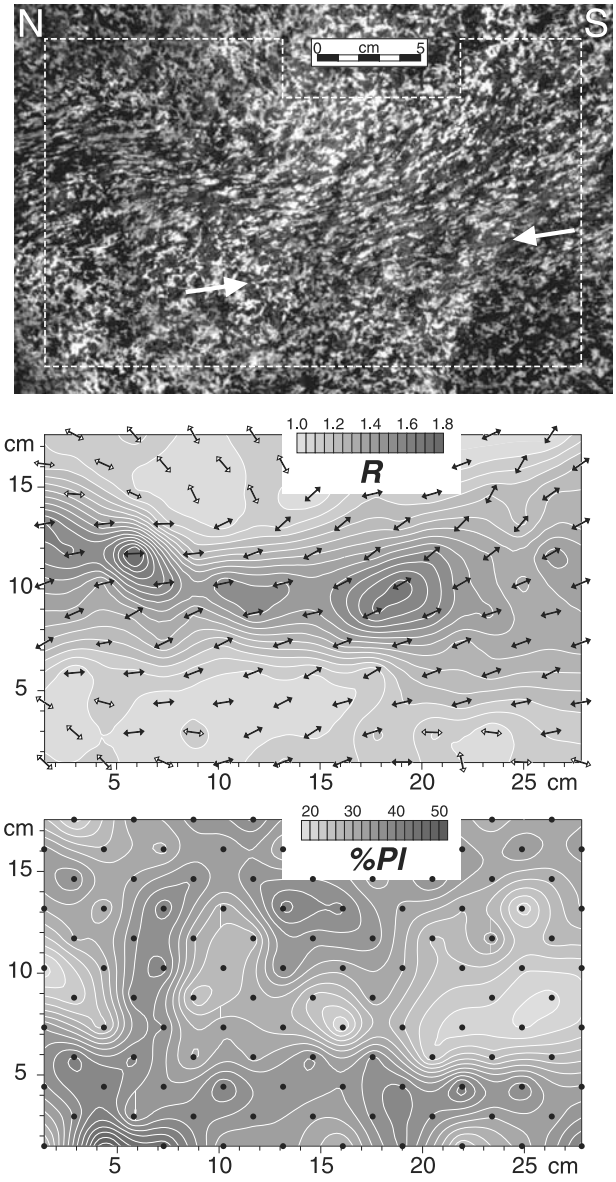

Figure 5. ASZ 57 shear zone. (top) [*XZ*] field image (location in Figure 3; image properties in Table 1). White arrows point to a thin, late magmatic, felsic vein that crosscuts the earlier ASZ 57 shear zone. Dashed white square delimits the area used for *R* and %Pl mapping. (middle) Strain ratio *R* map. Double arrows parallel the local plagioclase shape fabric direction α at centers of each analyzed image. Double white arrows are preserved magmatic fabric. (bottom) A %Pl map. Black dots are centers of analyzed images. Calculation using the INTERCEPT.EXE program [*Launeau and Robin*, 1996]. Angular counting step is 9° in a circular window.

quartz-plagioclase-garnet-bearing segregation veins pointing to temperatures exceeding 650°C under pressure >0.8 GPa. The ductile strain localization initiated at a magmatic stage dated at 98.9 ± 0.4 Ma (U/Pb age [*Schaltegger et al.*, 2002]) and propagated to form the anastomosing pattern until at least 83 Myr ago, the minimum age of retrograde amphibolite facies conditions [*Treloar et al.*, 1989].

[4] Bordering strain gradients of four shear zones have been investigated (Figure 1a and Table 1). These shear zones have been selected because they record different amounts of finite strain, which are interpreted as successive development stages. These differently oriented mylonites (Figure 3) crop out in sections perpendicular to foliation and parallel to the stretching direction, i.e., the [*XZ*] plane of finite strain [e.g., *Ramsay*, 1980], also called vorticity profile plane [*Robin and Cruden*, 1994; *Passchier*, 1998]. Strain measurements were carried out on this plane. The three-dimensional (3-D) fabric analysis was performed on oriented samples cut along [*XZ*], [*YZ*], and [*XY*] planes of finite strain.

2.1. ASZ 1

[5] The flat-lying ASZ 1 shear zone includes a 0.9–1.2 m wide mylonite zone bordered by 15-cm-wide strain gradients (Figure 3). The wall gabbro shows a very weak foliation inclined by about 70° to the shear zone orientation, taken as the mylonite border. In the footwall, the gabbro-welded fragments of a hornblendite vein indicates subcoeval emplacement of the hornblendite dike and the gabbro. Three differently oriented, centimeter-thick felsic veins bordered by euhedral garnets crosscut both the gabbro and the hornblendite. Shear deformation has bent all veins along with the primary gabbro foliation. The thickness of the veins is drastically reduced in the mylonite (Figure 4).

2.2. ASZ 3

[6] The ASZ 3 profile straddles the upper, sharp boundary of a nearly isotropic gabbro lens (Figure 3). The shear zone splits into two branches isolating a decimeter-big lens of weakly sheared gabbro. The near absence of strain gradient may originate from the small angle between the mylonite and the primary foliation preserved in the core of the gabbro lens. The potential influence of the orientation of the protolith shape fabric on development of strain gradients will be quantified by comparing strain at the border of this shear zone with gradients of ASZ 1 and ASZ 4.

2.3. ASZ 4

[7] The ASZ 4 shear zone illustrates one of the complex geometries observed in the area. The shear zone progressively curves and thins lengthwise from the steep (upper right corner, Figure 3) to the flat (lower right corner, Figure 3) boundaries of a 2-m-long lens of weakly deformed gabbro. Increasing shear strain from the steep to the flat parts of the mylonite is suggested by the boudinage and disintegration of quartz-feldspar veins, which become isolated porphyroclasts in the thinner mylonite zone. The gabbro lens displays antithetic shear bands (Figure 3), which may reflect within-lens deformation that accommodates strain imposed at boundaries between interfering and relatively stiff lenses.

2.4. ASZ 57

[8] The ASZ 57 shear zone is a few centimeters thick and about 20 cm long. It bends the trace of the gabbro foliation and did not develop mylonite (Figure 5). This type of shear zone has preserved the magmatic assemblage throughout and exemplifies incipient, high-temperature strain localization in the gabbro [*Arbaret et al.*, 2000]. ASZ 57 documents how shear zones die out in the protolith.

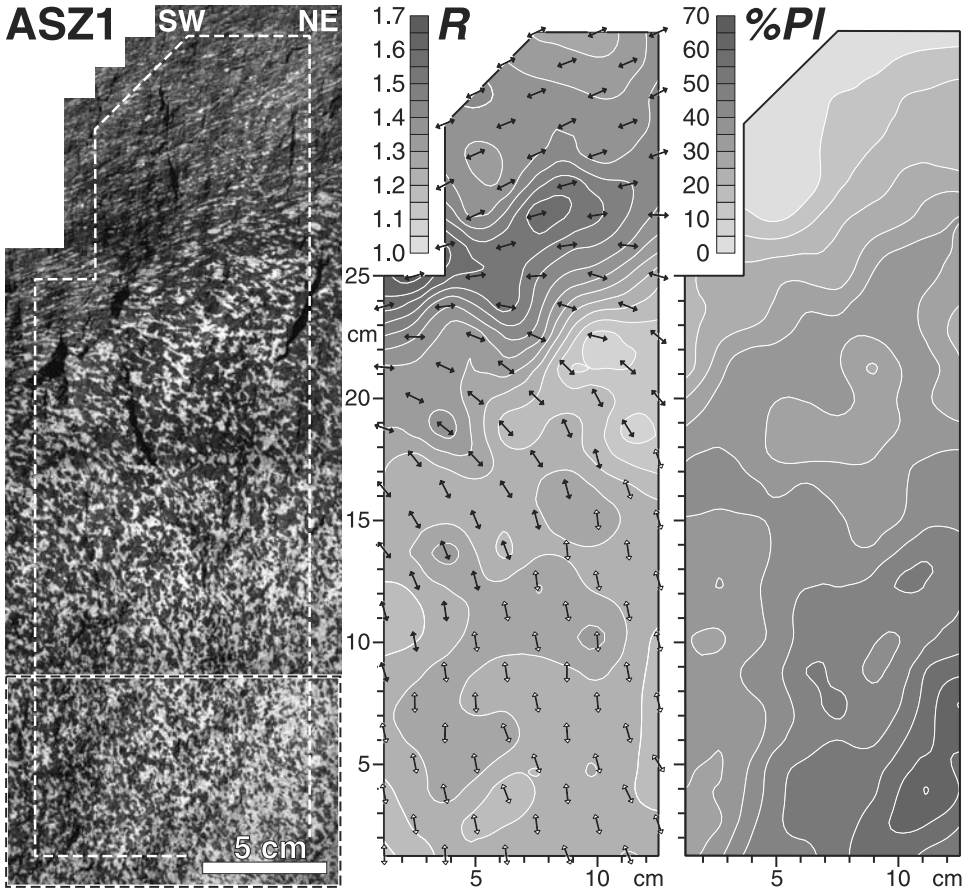

Figure 6. (left) Analyzed field image of ASZ 1 [*XZ*] surface (location in Figure 3; image properties in Table 1). All symbols in *R* map (middle) and %Pl map (right) and calculation procedure are as in Figure 5. Note the plagioclase-rich, patch-like zone at the bottom right of the photo and %Pl map. Black dashed square at the bottom of the photo denotes reference image used for numerical deformation.

[9] In shear zones ASZ 1, 3, and 4, the contact between the protolith gabbro and the mylonite zone is defined by a markedly smaller grain size associated with a shape fabric parallel to the general orientation of the mylonite zone. This contact, hereafter called mylonite border, is used as the referential in fabric and strain analyses.

3. Two-Dimensional (2-D) Shape Fabrics

[10] The protolith gabbro comprises light color feldspar and dark pyroxene/amphibole. Grains are approximately equidimensional on any outcrop orientation and become elliptical within [*XZ*] planes of strain gradients. The fabric was measured using the intercept method, which analyzes boundaries of objects with unique characteristics as a population of lines. The method involves a Fourier series decomposition of the polar plot of intercepts and yields a rose of directions, which quantifies the fabric symmetry, its direction α (in this study, with respect to the orientation of the mylonite border), and its intensity expressed by the strain ratio *R* [*Saltikov*, 1958; *Launeau et al.*, 1990; *Launeau and Robin*, 1996]. Our results actually quantify the shape fabric of feldspars, the weakest mineral phase in the gabbro. Images were divided into 500 × 500 pixel images following a diamond-shaped grid (arrows in Figures 5–8 are at image centers). Fabric measurements and surface percentage (%Pl) maps were obtained from a mosaic of the 500 × 500 pixel images.

[11] The shape of individual grains depends on several factors including local strain and deformation mechanisms. The feldspar grain shape is not the finite strain ellipse because weakest phases deform more than a theoretical marker. However, differences in directions and shapes obtained by the intercept method give a semiquantitative indication of strain variations.

3.1. ASZ 1

[12] Plagioclase forms 33.2% ± 5.2 of the imaged wall protolith (Figures 6 and 9c). This content increases to %Pl = 48.2% ± 9 in patch-like zones, with a maximum %Pl = 62% (Figure 6). The plagioclase percentage begins to decrease at about 7 cm from the mylonite border along which %Pl < 15%. Plagioclase-rich zones are common in the gabbro whose feldspar-shape fabric has a consistent direction $\alpha = 103° \pm 7$ and strain ratio $R = 1.23 \pm 0.04$, independent of the local variation in plagioclase content (Figure 9). Fourteen centimeters away from the mylonite border, the primary fabric begins turning into the strain gradient. The strain ratio decreases to $R < 1.1$, as the direction α becomes subperpendicular to the shear zone.

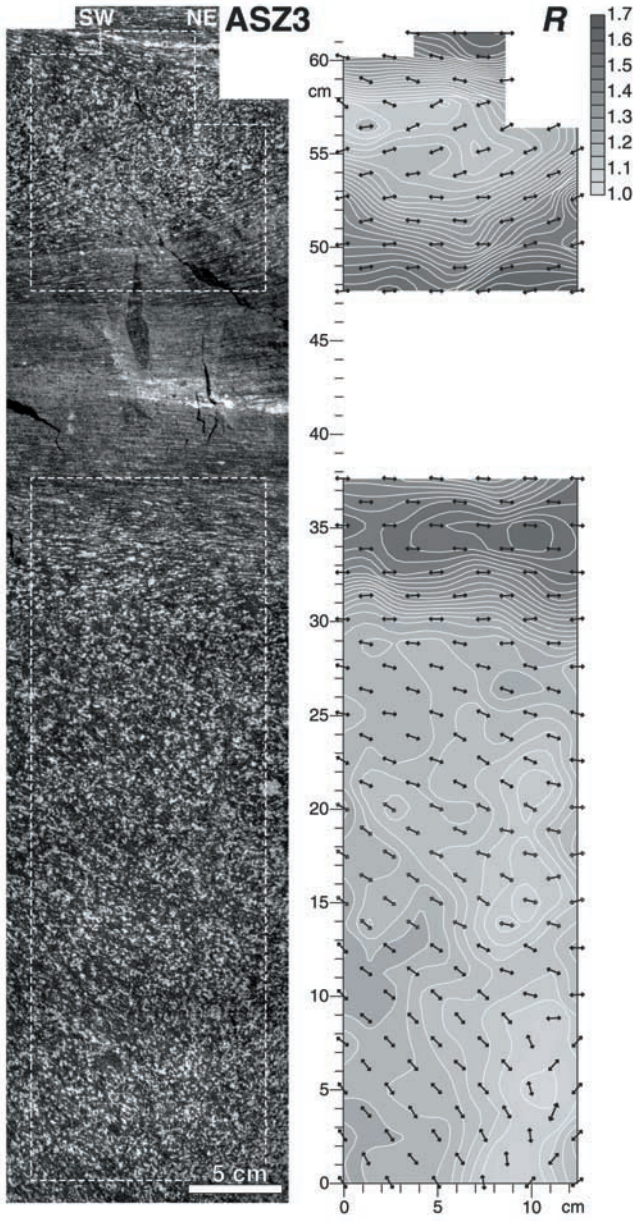

Figure 7. ASZ 3 shear zone. (left) Analyzed [*XZ*] field image (location in Figure 3; image properties in Table 1). (right) *R* and %Pl maps. All symbols in *R* map and calculation procedure are as in Figure 5.

The strain ratio then increases to reach $R = 1.55$ along the mylonite border (Figure 9b).

[13] The mylonite zone is characterized by a homogeneous direction $\alpha = 1.0° \pm 2.4$ and a stable strain ratio $R = 1.36 \pm 0.04$ (Figures 6 and 9). This strain ratio is lower than the maximum in the strain gradient but remains higher than the average ratio in the gabbro. The plagioclase percentage is low, locally <5% but is underestimated because some grains are too small to be detected.

3.2. ASZ 3

[14] In the gabbro next to this shear zone, the plagioclase percentage is regular, with an average of %Pl = 28.2% ± 3.9 (Figures 7 and 9c). Similar to ASZ 1, this average value is constant up to about 7 cm away from the mylonite border. The strain ratio is on average $R = 1.16 \pm 0.06$ up to 14 cm from the mylonite border toward which it then increases within the strain gradient (Figure 9b). At 30–35 cm from the mylonite border, the main fabric direction $\alpha = 56.3° \pm 15.3$ is affected by a centimeter-scale shear zone along which α becomes perpendicular to the mylonite border (lower right part, Figure 7). The vicinity of two shear zones affecting together the shape fabric explains the apparent absence of fabric gradient at this place. From this shear zone to 5 cm from the mylonite border, the fabric direction decreases linearly. Between 5 and 0 cm from the border, the fabric direction is stabilized at $\alpha = 2.3° \pm 1.6$ (Figure 9a). In the

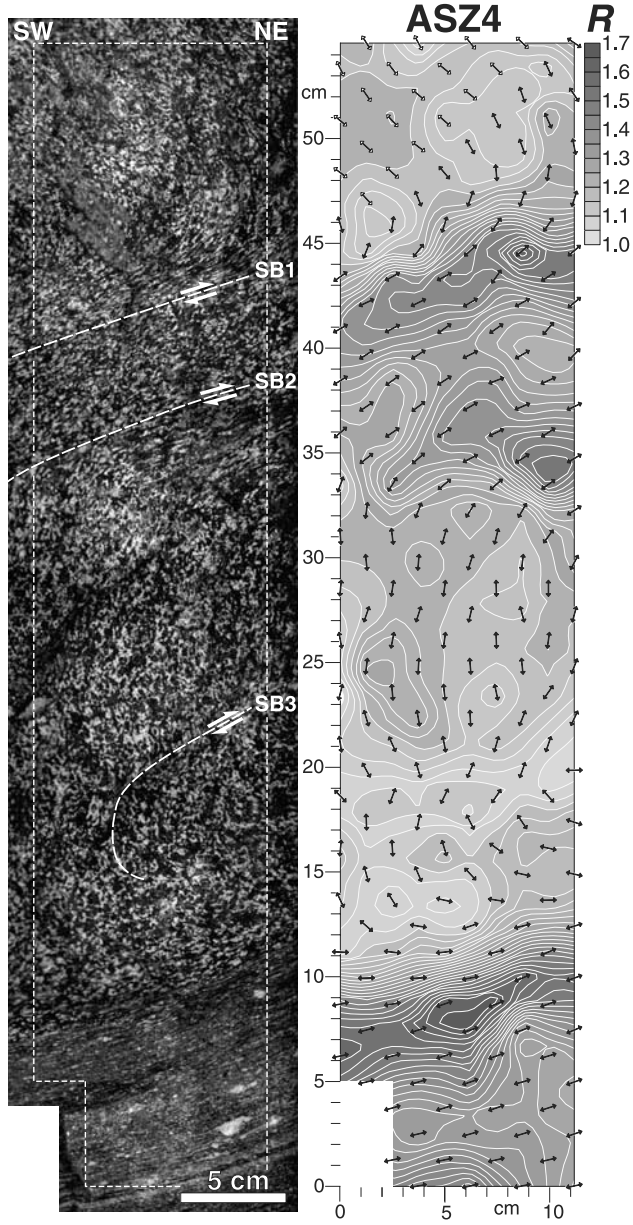

Figure 8. ASZ 4 shear zone. (left) Analyzed [*XZ*] field image (location in Figure 3; image properties in Table 1). (right) *R* and %Pl maps. All symbols in *R* map and calculation procedure are as in Figure 5. SB1, 2, and 3 are minor antithetic shear bands.

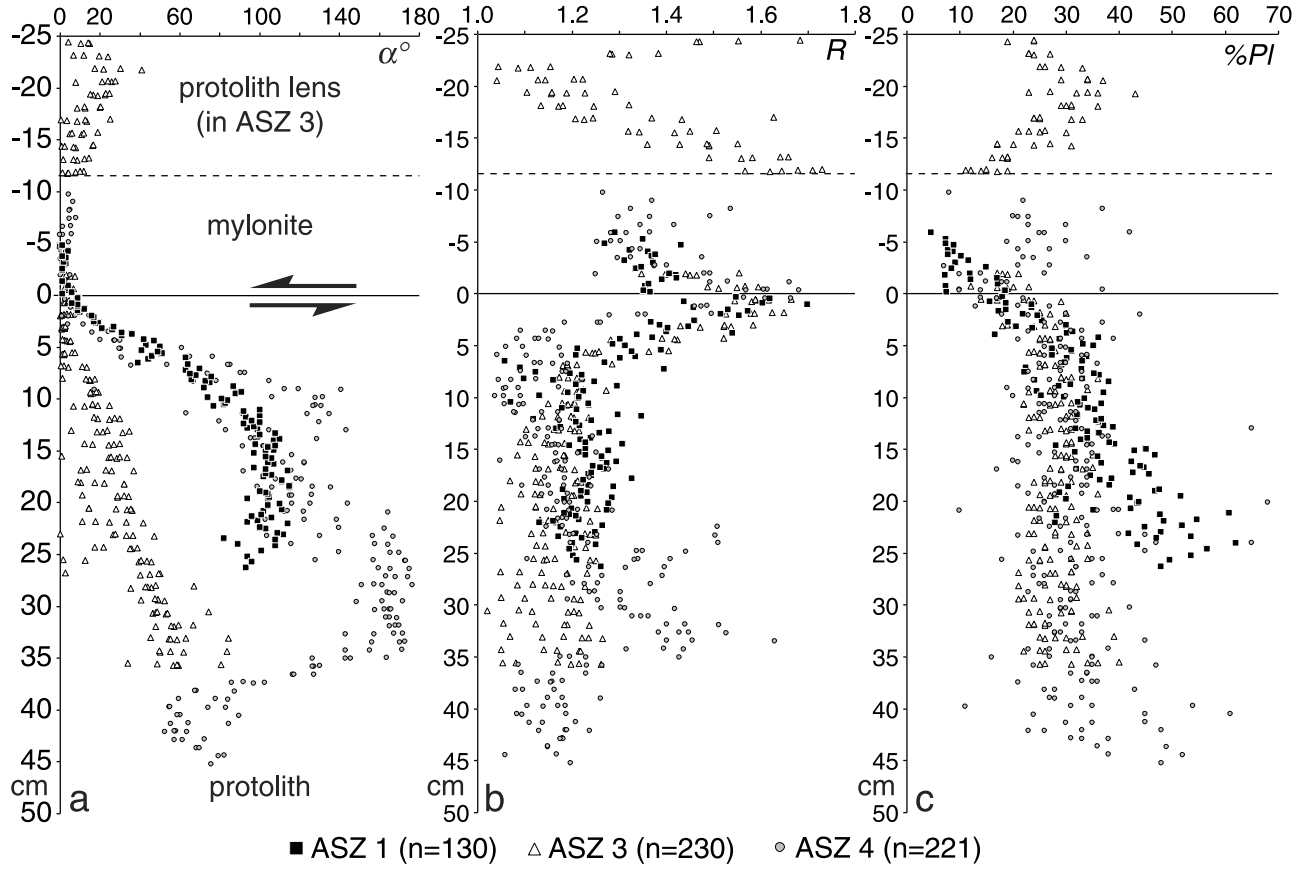

Figure 9. [*XZ*] evolutions of (a) the shape fabric direction α, (b) strain ratio *R*, and (c) surface percentage %Pl of plagioclase in ASZ 1, ASZ 3, and ASZ 4; *n* is number of measurements.

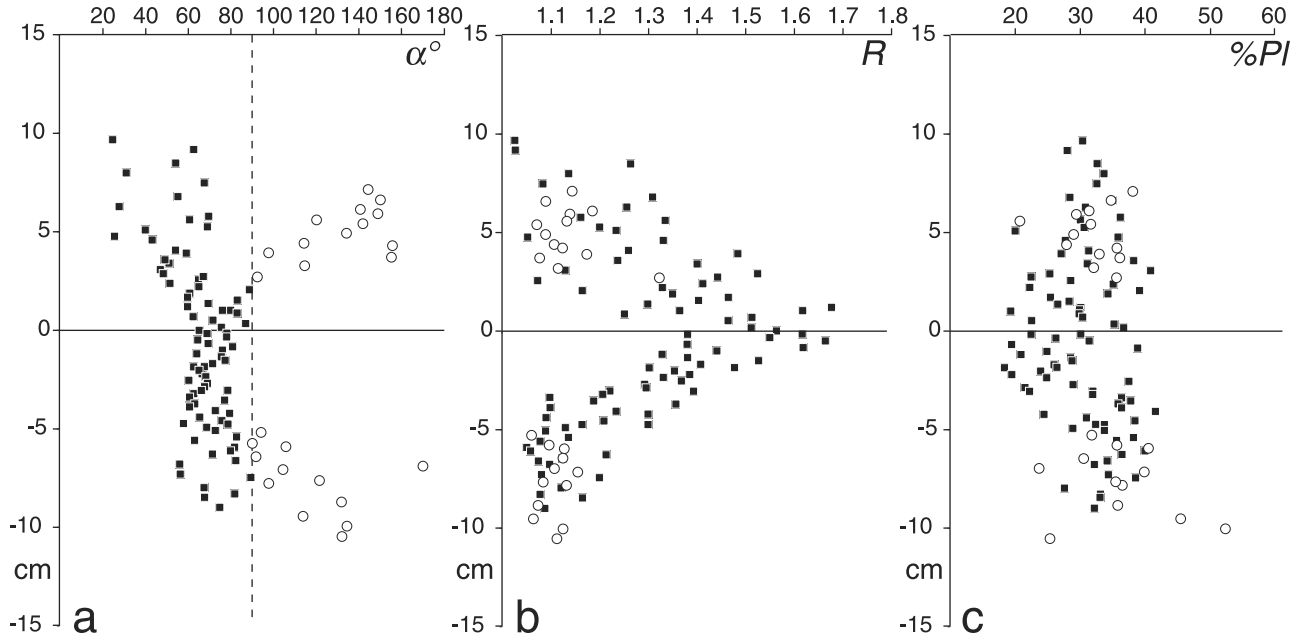

Figure 10. ASZ 57 shear zone: [*XZ*] evolutions of (a) the shape fabric direction α, (b) strain ratio *R*, and (c) surface percentage %Pl of plagioclase. The horizontal zero line marks the middle of the shear zone, i.e., highest strain ratios. The vertical dashed line in Figure 10a separates directions α of the magmatic fabric (white dots) from directions α in the strain gradient (black dots). Number of analyzed images is $n = 109$.

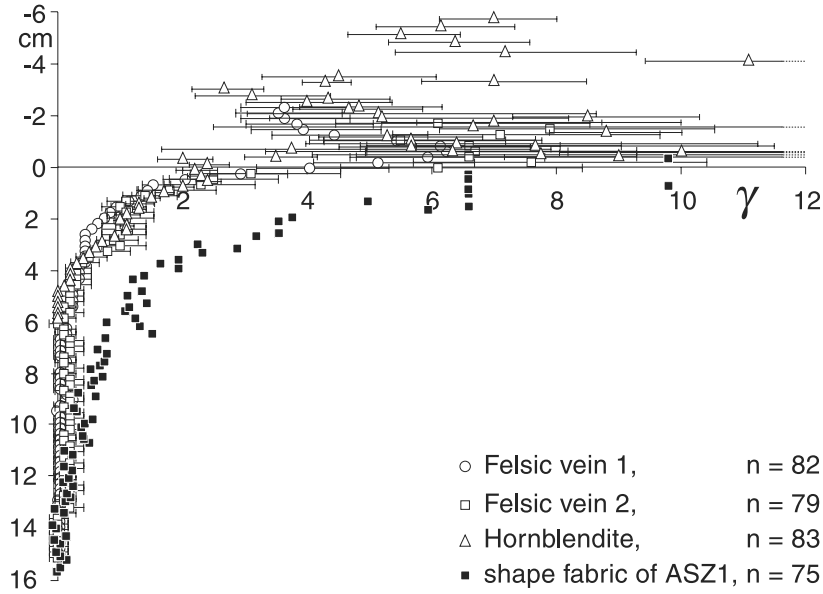

Figure 11. ASZ 1, Simple shear strain γ versus distance to the mylonite border. Black symbols denote γ calculated from the trace of the plagioclase shape fabric direction α assuming passive deformation. γ points calculated from α across ASZ 3 and ASZ 4 are hidden below the white symbols γ calculated from the bending of the felsic and hornblendite veins. The ASZ 3 and ASZ 4 measurements are displayed in Figure 12.

mylonite zone, the direction $\alpha = 4.0° \pm 1.9$ and the strain ratio $R < 1.35$ are nearly the same as in the ASZ 1 mylonite. However, the percentage of plagioclase is slightly higher (average %Pl = 18.2% ± 2.8; Figure 9c).

[15] The percentage and shape fabric of plagioclase have been analyzed in the size-size lens included within the mylonite zone (Figures 7 and 9). From both mylonite borders to the center of this lens, the direction α increases

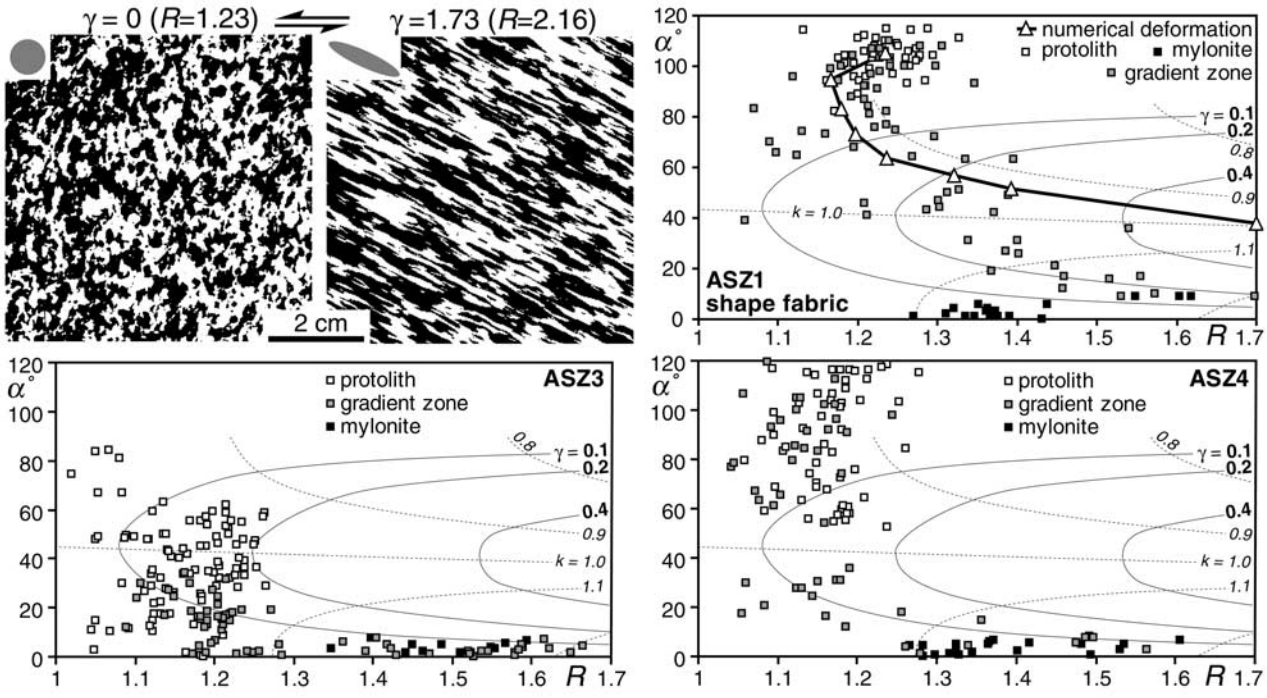

Figure 12. (top left) Binarized bottom part of Figure 6 used as reference γ = 0 for ASZ 1 and its numerical deformation to γ = 1.73. White denotes plagioclase; black denotes pyroxene + amphibole + oxides. Grey ellipse denotes theoretical *XZ* strain ellipse. The α/*R* diagrams [*Tikoff and Fossen*, 1993] document the relative importance of simple shear (γ) and pure shear surface loss (*k*) in the respective shear zones. See discussion in the text.

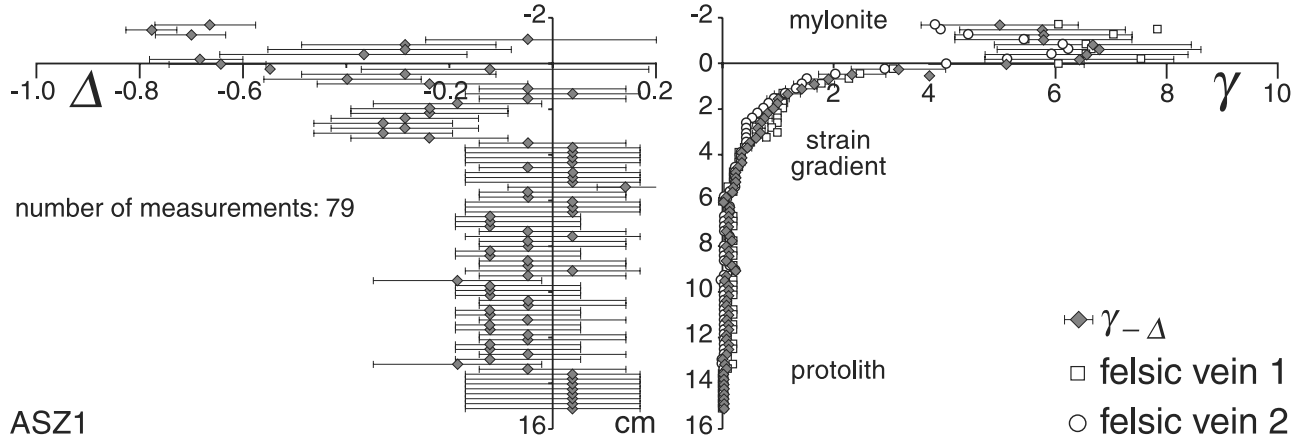

Figure 13. Evolution of volume loss Δ and simple shear strain $\gamma_{-\Delta}$ components in the ASZ 1 shear zone calculated from passive deflection of the felsic veins (Figure 3). White symbols denote γ from Figure 12.

from about 0° to 41° (Figure 9a), whereas the strain ratio R decreases from more than 1.7 to less than 1.1 (Figure 9b). The plagioclase content, which is minimum along the mylonite borders at %Pl = 11%, is 43% in the center of the lens (Figure 9c), which has thus preserved protolith characteristics.

3.3. ASZ 4

[16] The primary fabric of the gabbro, 37 cm from the shear zone (white arrows in Figure 8), has an average direction $\alpha = 68.8° \pm 11.5$ and a strain ratio $R = 1.15 \pm 0.05$, while the plagioclase proportion averages %Pl = 36% ± 11 (Figure 9). Along the two upper, antithetic shear bands SB1 and SB2 (Figure 8) and in between, the direction α becomes parallel to the mylonite border with a strain ratio R increasing to more than 1.52 in both bands. The strain ratio in the SB3 shear band is <1.04. This low ratio is related to strain interference of opposed senses of shear between SB3 and ASZ 4 (Figure 8). Despite the influence of SB3, both R and %Pl evolve across ASZ 4 in a similar manner as across ASZ 1. In the mylonite, the plagioclase fabric is almost parallel to the shear zone direction ($\alpha = 1.5° \pm 3.4$) and has a strain ratio of $R = 1.41 \pm 0.12$ (Figure 9). The plagioclase percentage has a large standard deviation in this mylonite with %Pl = 22% ± 9. Maximum local values of %Pl = 42% are correlated with the presence of size-size plagioclase porphyroclasts derived from disaggregated felsic veins (Figure 3).

3.4. ASZ 57

[17] This shear zone represents lengthwise-terminated discrete zones without a central mylonite zone (Figure 5). The primary shape fabric has a homogenous strain ratio $R = 1.12 \pm 0.05$ (Figure 10b) and a homogeneous foliation direction $\alpha \approx 65°$ (white double arrows in R map, Figure 5). The primary foliation progressively turns into nearly symmetric strain gradients (Figures 5 and 10a). The plagioclase percentage is scattered from 21 to 53% with an average of %Pl = 35% ± 7 (Figure 10c).

[18] With no mylonite border, the reference line is taken as the regularly oriented trend made by the maximum values of $R = 1.68$ (Figure 5). Approaching this reference line, the fabric direction becomes $\alpha = -17.5° \pm 7.9$ (Figure 10a). The plagioclase percentage decreases to %Pl = 18.5% (Figure 10c). It is worth noting that the smallest %Pl does not match the maximum strain ratio because strain localization took place along the border of plagioclase-rich domain. Therefore the distribution of the weakest mineralogical phase seems to play a vital role in strain localization [*Goodwin and Tikoff*, 2002].

3.5. General Evolution

[19] The four shear zones illustrate different geometries in the same anastomosed network. Yet a general evolution from the protolith gabbro to mylonite can be recognized from the 2-D [*XZ*] variations of feldspar-shape fabrics. The trace of the primary foliation is similarly bent in meter- to centimeter-thick strain gradients, which indicate that the process is scale-independent. The strain ratio R evolves in a manner similar to maximum values of about 1.70 at the mylonite borders, where the plagioclase percentage is at a minimum (%Pl < 20%). Plagioclase-rich zones were crucial in the strain localization process.

[20] In the mylonites, the fabric direction α is nearly parallel to the mylonite border. The strain ratio R is stable (about 1.35) at more than 2 cm from the protolith. The plagioclase percentage varies depending on the presence of partly or totally disaggregated felsic veins.

4. Shear Strain Analysis

[21] A strain analysis could be performed in the [*XZ*] planes of finite strain (1) using the angular relation of the foliation to the boundary of the ASZ 1, 3, and 4 mylonites and (2) computing deflection of the hornblendite and felsic veins deformed into ASZ 1.

4.1. Simple Shear Hypothesis

[22] The simplest strain technique considers that the foliation in [*XZ*] planes of shear zones traces the direction of the long axis of the finite strain ellipse. Assuming ideal simple shear, simple shear strain γ is represented by [*Ramsay and Graham*, 1970]

$$\gamma = 2/\tan(2\alpha). \quad (1)$$

Table 2. Whole Rock Analysis of Major (Measured and Normalized) and Trace Elements Measured by Inductively Coupled Plasma Mass Spectrometry on Samples From Both the Protolith Gabbro and the Mylonite of ASZ 1[a]

	Protolith	Mylonite
	Major Elements, wt %	
SiO_2	52.29	53.56
Al_2O_3	17.96	17.73
Fe_2O_3	9.68	9.41
MgO	5.16	4.5
CaO	9.87	9.54
Na_2O	2.58	2.91
K_2O	0.37	0.27
TiO_2	0.72	0.76
P_2O_5	0.13	0.13
MnO	0.16	0.15
LOI	0.91	0.86
Total	99.83	99.82
	Normalized Major Elements, wt %	
SiO_2	52.37	53.65
Al_2O_3	17.99	17.76
Fe_2O_3	9.69	9.42
FeO	5.16	4.50
MgO	9.88	9.55
CaO	2.58	2.91
Na_2O	0.37	0.27
K_2O	0.72	0.76
TiO_2	0.13	0.13
P_2O_5	0.16	0.15
MnO	0.91	0.86
Total	100.00	100.00
	Trace Elements, ppm	
Ba	137.0	79.5
Ce	11.4	12.4
Co	29.5	26.8
Cr	62.2	46.2
Cu	37.2	55.7
Dy	3.15	2.96
Er	1.97	1.88
Eu	1.08	0.87
Ga	17.7	16.8
Gd	2.88	2.55
Ge	1.70	1.39
Hf	1.07	1.30
Ho	0.672	0.642
La	5.10	5.54
Lu	0.335	0.277
Nb	0.98	1.15
Nd	7.75	8.31
Ni	14	10
Pb	42.8	47.6
Pr	1.64	1.70
Rb	3.14	1.13
Sm	2.34	2.32
Sn	0.55	0.60
Sr	259	262
Ta	0.07	0.09
Tb	0.469	0.442
Th	0.39	0.40
Tm	0.307	0.278
U	0.14	0.11
V	244	275
Y	19.4	17.5
Yb	2.05	1.82
Zn	83.8	78.9
Zr	33.1	46.1

[a]Analyses performed at the CRPG-Nancy, France.

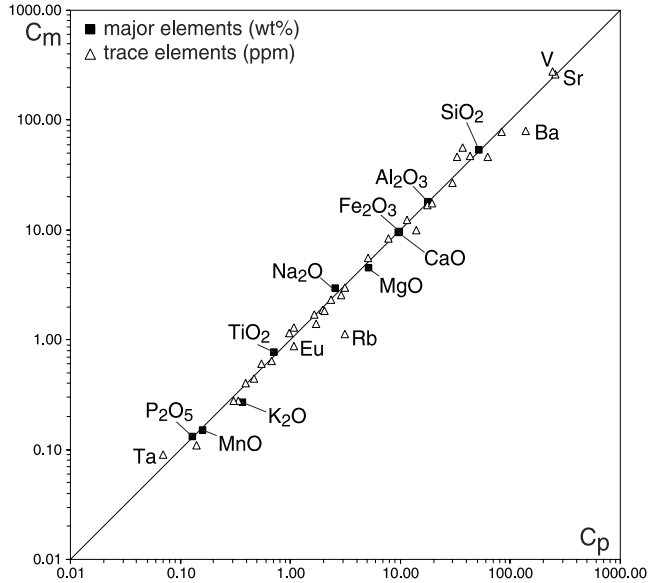

Figure 14. Isocon diagram comparing major and trace elements concentrations (Table 2) in the mylonite (C_m) and in the protolith (C_p).

We used the measured direction α in equation (1). The shear strain versus distance curves across the ASZ 1, 3, and 4 strain gradients (Figure 11) vary from zero, within the protolith, and typically become asymptotic to infinite values of γ in the mylonites because the fabric directions α become near-parallel to the mylonite walls.

[23] An independent measure of the shear strain can be obtained from the deflection of three veins with different initial orientations within the ASZ 1 shear zone. The local shear strain γ is calculated from the mathematical expression [*Ramsay*, 1980]:

$$\gamma = \cot \delta' - \cot \delta, \tag{2}$$

where δ is the initial orientation of the vein in the protolith gabbro and δ' is the deformed orientation, i.e., the slope between two successive digitized points of the deflected veins with respect to the reference mylonite border (Figure 3). The regular digitalization step was 0.215 cm along the felsic veins. Five centimeters away from the mylonite border, the NE margin of the hornblendite is very irregular and was therefore excluded for strain calculation. A similar variation of γ is obtained within the range of errors from both felsic and hornblendite veins (Figure 11). This similarity indicates that viscosity contrasts between all veins, and the screening gabbro was low enough to allow passive deformation [*March*, 1932].

[24] In mylonite, the large spread of shear strains calculated from all veins ($2 < \gamma \gg 12$ average $\gamma = 7.2 \pm 3.5$; Figure 11) reflects the imperfect initial shape of the veins combined with large errors in measuring small angles between shear zone boundary and veins. For example, γ calculated from the felsic vein 1 varies from $\gamma = 6$ to $\gamma = 3.5$ within the mylonite.

[25] Now we compare the evolution of γ calculated independently from equations (1) and (2). The shape strain

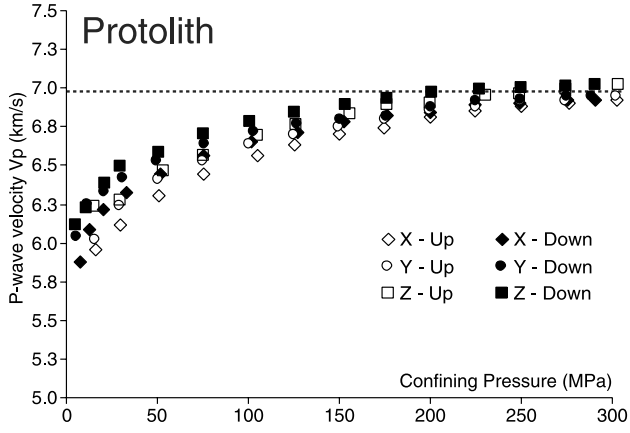

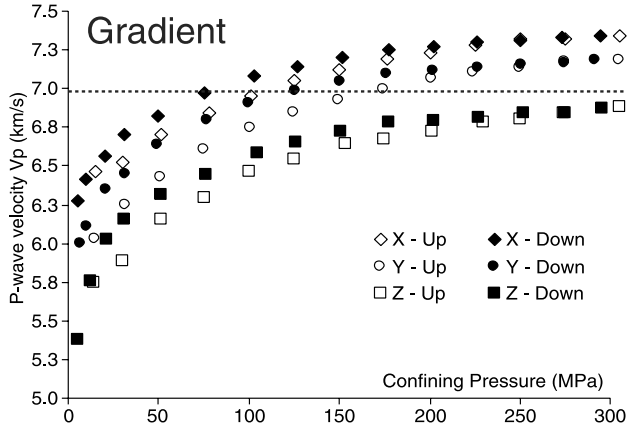

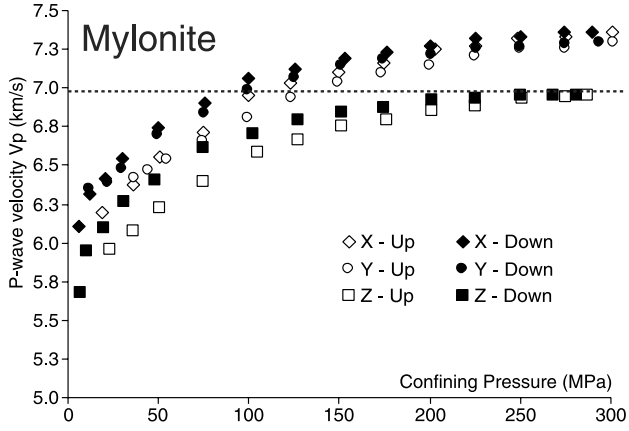

	Protolith	Gradient	Mylonite
Vp (km/s)	7.090	7.135	7.202
Density (kg/m^3)	2.997 ± 0.012	3.049 ± 0.007	3.081 ± 0.007
Anisotropy (%)	-1.283	6.391	5.633

Figure 15. *P* wave velocity V_p versus confining pressure for three orthogonal directions parallel to the reference axes defined as *X* the stretching lineation and *Z* normal to the [*XY*] mylonite foliation. Horizontal dashed line denotes average V_p of the protolith measured at 300 MPa. Lowest *P* waves anisotropy $A = -1.283\%$ in the protolith, maximum $A = 6.391\%$ in the gradient zone, and intermediate $A = 5.633\%$ in the mylonite. Fastest *P* waves are normal to [*XY*] but near parallel to the protolith foliation, inducing negative calculated anisotropy.

gradient begins 14 cm from the mylonite, whereas the strain gradients from veins begin only about 6 cm from the mylonite border (Figure 11). This difference indicates that the assumption of ideal simple shear is not valid or that the measurement techniques are not reliable. Indeed, oriented crystallization of pargasite and quartz progressively replacing primary plagioclase and pyroxene results in grain-size reduction. Furthermore, new crystals exhibit lower aspect ratios than plastically deformed plagioclase. Therefore new crystals impart a lower strain ratio and a fabric direction closer to the mylonite border than expected from theoretical passive deformation of isolated plagioclase grains.

4.2. Nonideal Simple Shear Hypothesis

[26] To test the ideal simple shear hypothesis, we compared virtual fabrics obtained from numerical simple shear deformation of the pictured protolith gabbro (location in Figure 6) with measured shape fabrics in ASZ 1 (Figure 12). For this purpose, we used the α/R diagram, which also gives the simple shear (γ) and pure shear surface loss (k) components [*Tikoff and Fossen*, 1993]. The numerical fabrics plot on a curve that starts at $\alpha_{num} = 103°$ and $R_{num} = 1.23$ (the protolith fabric). This numerical curve makes a loop toward smaller α_{num} and R_{num} values before downsloping toward higher R_{num} values on the line $k = 1$ of ideal simple shearing of an initially isotropic fabric (Figure 12). This simulation allows the distinction of two subzones in the actual strain gradient. For $0 < \gamma < 0.2$, shape-fabric measurements are distributed along or near, and follow the simulation α/R curve. This fit suggests that strain is accommodated by near-ideal simple shear of the crystalline aggregate from the protolith into the low-strain part of the shear gradient. Measured fabric points plot significantly away from the simulation curve once $\gamma > 0.2$. In particular, points near the mylonite border plot at $1.15 < k < 1.25$, which indicates a pure shear and/or surface loss component in high-strain domains. The same conclusions are reached for ASZ 3 and ASZ 4 (Figure 12). We conclude that the high-strain shape fabric does not reflect simple shear of the crystalline aggregate.

[27] The shape fabric measurements detect strain at a larger distance from the mylonite border than the deflection of veins. This supports the point that felsic veins emplaced during the development of strain gradients and were deformed by continued shear, which took place during the

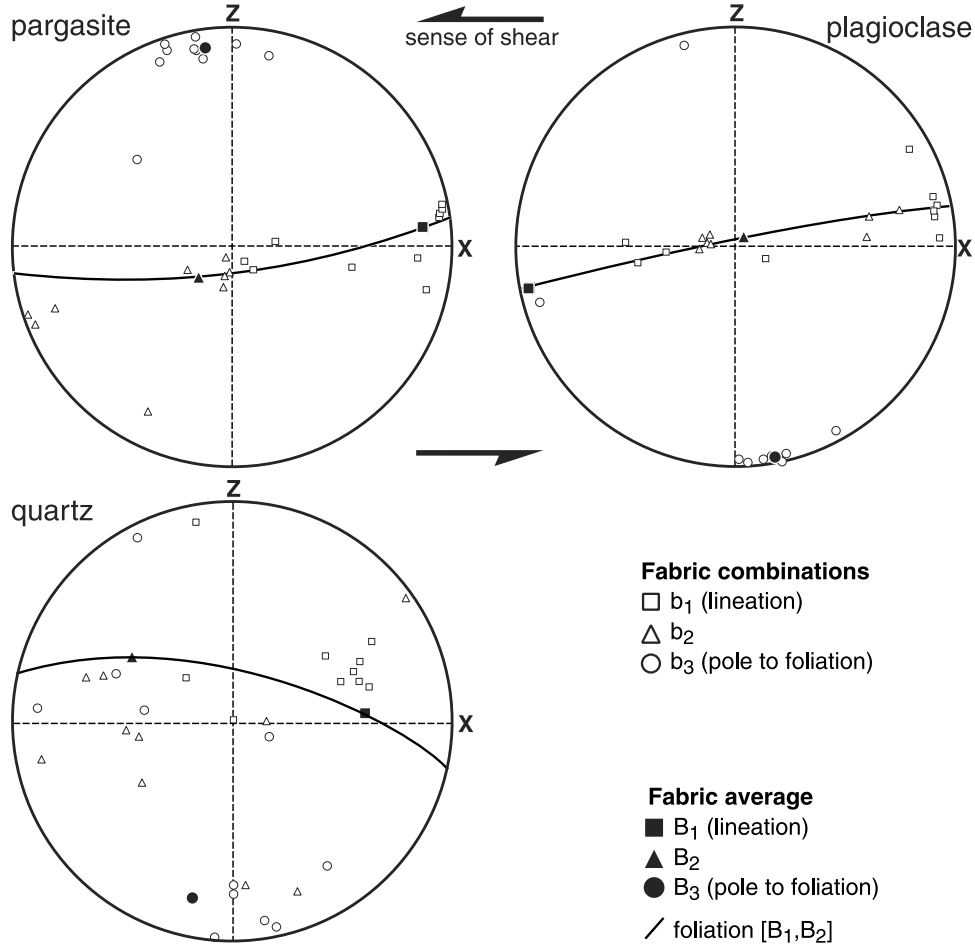

Figure 16. Lower hemisphere pole figures of SPO calculated by combining [*XZ*], [*YZ*], and [*XY*] fabric ellipses (intercept method [*Launeau and Robin*, 1996; *Robin*, 2002]). White symbols denote measured fabrics. Black symbols denote calculated average.

waning magmatic stages in the country gabbro [*Arbaret et al.*, 2000].

4.3. Surface Loss Calculation

[28] When two differently oriented passive markers such as veins are sheared, the surface change component Δ acting normal to the shear zone can be separated from the shear strain component $\gamma_{-\Delta}$ from

$$\gamma_{-\Delta} = \frac{\cot\delta\cot\beta' - \cot\beta\cot\delta'}{\cot\delta' - \cot\beta'} \quad (3)$$

and

$$\Delta = \frac{\cot\delta - \cot\beta}{\cot\delta' - \cot\beta'} - 1 \quad (4)$$

in which β and δ are the initial orientations, and $\beta'$and δ' are the final orientations of the veins [*Ramsay*, 1980].

[29] Equations (3) and (4) applied to the deflected felsic veins in ASZ 1 yield the shear strain $\gamma_{-\Delta}$ and the surface loss Δ. The shear strain component $\gamma_{-\Delta}$ appearing at 6 cm from the mylonite border exponentially increases to reach $\gamma_{-\Delta} = 6.1 \pm 0.6$ in the mylonite. Surface loss is detectable at about 3.5 cm from the mylonite border (Figure 13). In the

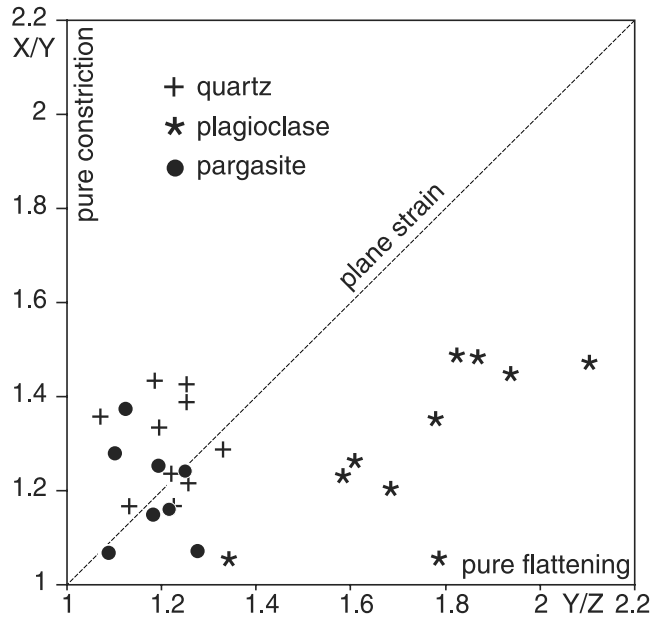

Figure 17. Shape fabrics from Figure 16 plotted in the Flinn diagram, which describes the shape of strain ellipsoids [*Flinn*, 1965].

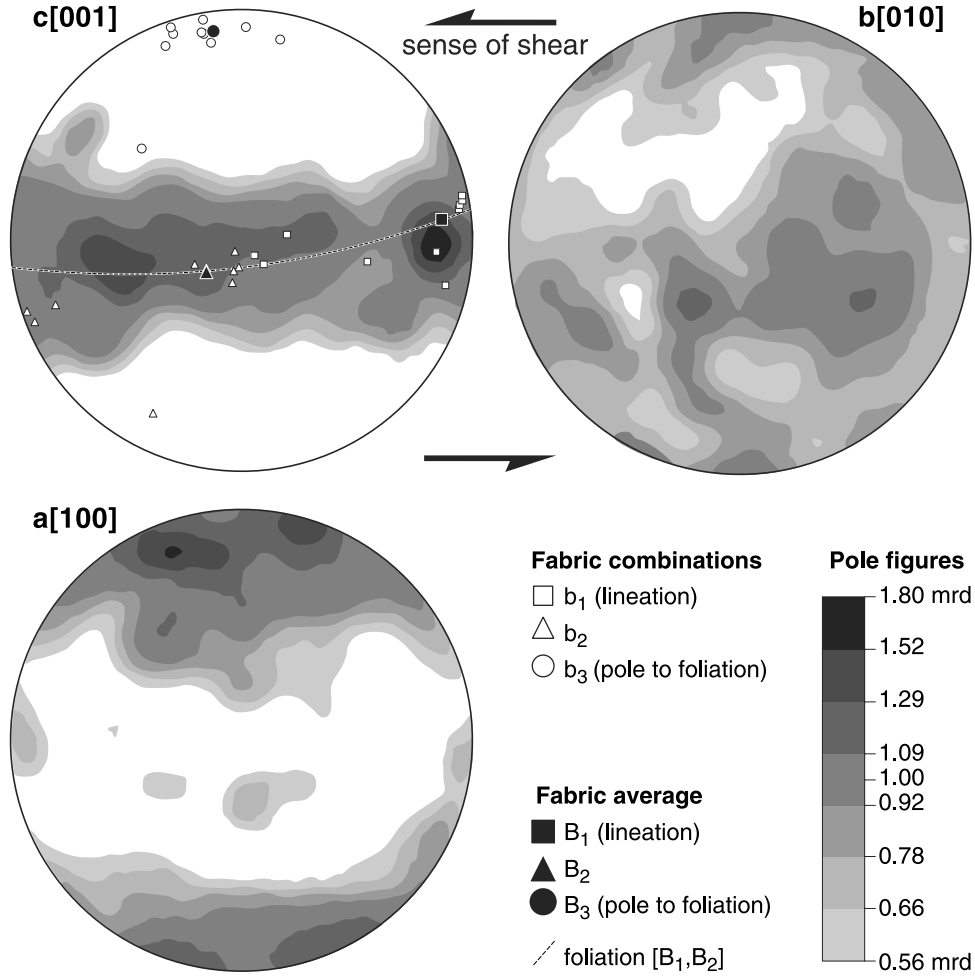

Figure 18. Lower hemisphere pole figures obtained from EBSD measurements on pargasite in the ASZ 1 mylonite, 2 cm from the mylonite border. [*XZ*] plane parallel to the projection surface with *X* horizontal. EBSD patterns were collected using the ETH-Zürich SEM CamScan CS44LB with an accelerating voltage of 15 kV. Indexing procedure was done using the software OIM 2.0 (TSL Inc.) and was based on a defined reference file of 20 reflections for the solid-state solution series of monoclinic amphiboles within the range of pargasite to tchermakite composition (unpublished).

mylonite, $8\% \leq \Delta \leq 80\%$ with an average at $\Delta = 48\% \pm 26$. The $\gamma_{-\Delta}$ variation is readily different in shape from the γ variation calculated on the same veins with equation (2) (Figure 11). This difference illustrates the technique sensitivity. At a high strain, small digitalization and measurement errors produce dramatic uncertainties.

5. Three-Dimensional Fabrics

[30] Grain-size reduction and recrystallization of pargasite and quartz from symplectitic plagioclase and pyroxene [*Yoshino et al.*, 1998] (Figure 2) characterize the high-strain domains, including the mylonites. The 2-D surface loss and/or pure shear component recorded in the high-strain domains correspond to sites where metamorphic reactions produced changes in OH-bearing phases (amphibole, epidote) and new garnet. Accordingly, metamorphic reactions involving volume changes should have produced changes in whole rock composition. Volume loss would also reflect the increase in density from protolith to mylonite assemblages induced by prograde metamorphism. We measured chemical compositions, 3-D seismic properties, and 3-D amphibole crystallographic and shape fabrics to discriminate these chemical, physical, and geometrical hypotheses.

5.1. Geochemical Analysis

[31] Volume changes in greenschist and amphibolite facies shear zones are often related to relative enrichment/loss of trace and major oxide elements enhanced by extensive fluid infiltrations [*O'Hara*, 1988; *Glazner and Bartley*, 1991; *Newman and Mitra*, 1993; *Ring*, 1999]. In particular, volume losses averaging 65.5% are attributed to fluid-rock interactions [*O'Hara*, 1994]. Up to 80% volume loss is inferred from the strain analysis of the ASZ 1 shear zone (Figure 13). To constrain this unexpectedly large estimate for near-granulite facies rocks, major and trace elements were measured on whole rock gabbro and mylonite samples (Table 2). The results are plotted on a conventional isocon line of constant concentration, a diagram that compares compositions of the two rocks [*Grant*, 1986]. Departure from the isocon line indicates relative enrichment/loss of elements according to their mobility [*Gresens*, 1967;

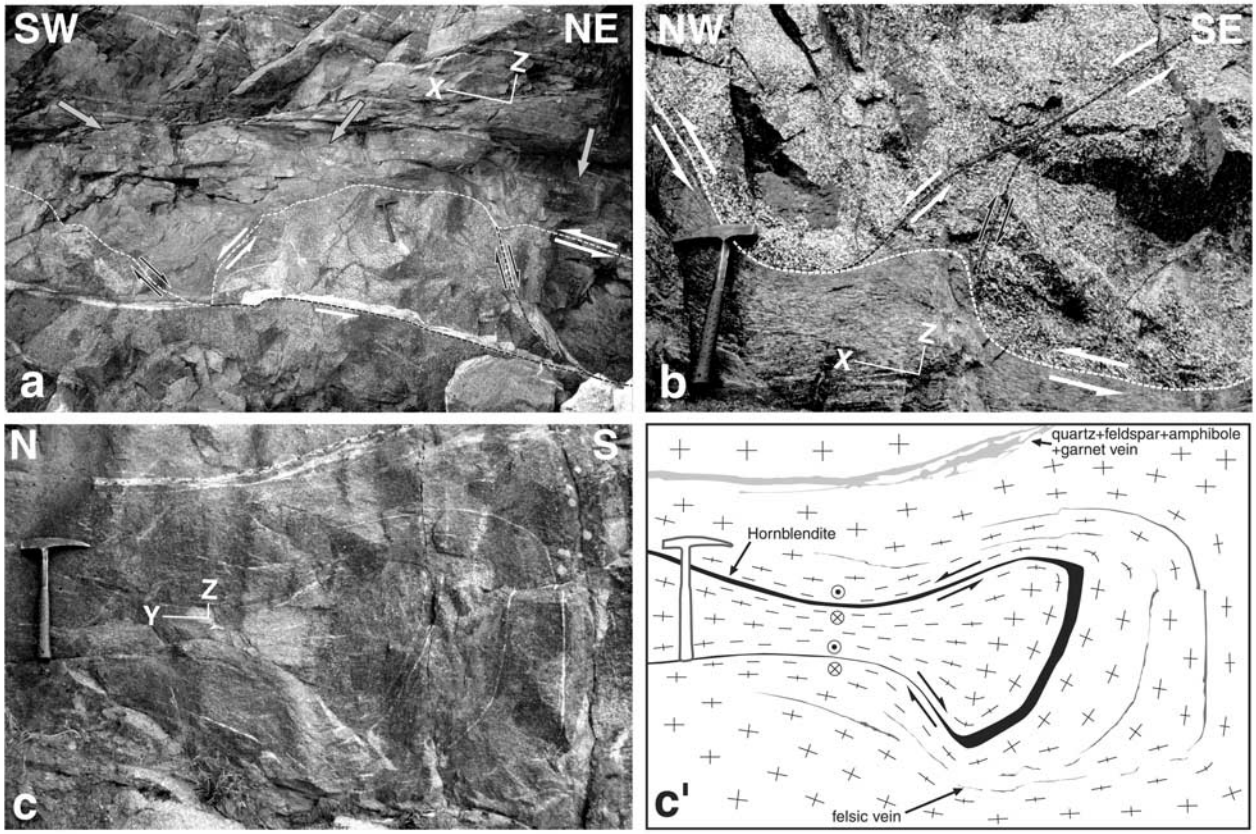

Figure 19. Complications in flow geometry. (a) Complex flow geometry in an SW vergent mylonite (white arrows) with antithetic normal shear zone splitting gabbro lenses (black arrows). The mylonite material seems to be sucked in between separating boudins. Grey arrows point to the linear trace of disaggregated feldspar veins showing that at this level the flow geometry remained undisturbed. (b) Extensional zone in a NW vergent shear zone (white arrows) with antithetic shear (black arrows) and accommodation folding of the mylonite into the extensional structure. (c) Photo and (d) sketch of a lens seen perpendicular to the stretching lineation of the surrounding mylonite. N-S, normal shear components (black arrows) on the flanks disturb westward shear (head/tail arrows). Note the outward and downward divergent foliation geometry at the south termination.

Newman and Mitra, 1993]. The major and trace elements of the gabbro and the mylonite of ASZ 1 all plot on, or close to, the line of constant concentration (Figure 14). Largest deviations for Ba or K_2O, for example, are negligible and insufficient to express even a small chemical mass transfer.

[32] Similar isochemical conditions associated with apparent volume loss derived from strain analysis have been reported in other ductile shear zones [*Srivastava et al.*, 1995; *Bhattacharyya and Hudleston*, 2001]. These authors invoked geochemical equilibration after deformation, but taking away and bringing back exactly the same amount of elements that have different mobilities seem to us more miraculous than natural. We prefer concluding that the isocon diagram (Figure 14) demonstrates that no migration was involved, either for major or for trace elements, and discard geochemical, fluid-assisted processes to explain the measured surface loss in the shear zone.

5.2. Seismic Properties

[33] Laboratory measurement of *P* wave velocity and their anisotropies were carried at room temperature and up to 300 MPa in a Heard-type pressure vessel using the pulse transmission technique [*Birch*, 1960; experimental technique by *Mauler et al.*, 2000]. Three perpendicular cores, 14.76 ± 0.01 mm diameter and 28.58–31.98 mm long each, were cut from the protolith, the gradient zone, and the mylonite of ASZ 1 along directions parallel to the main shape fabric axes in the mylonite: X_S core parallel to the mineral lineation, Y_S core normal to mineral lineation and parallel to foliation, and Z_S core normal to foliation.

[34] For the three rocks and all directions, the nonlinear increase of *P* wave velocities with confining pressure (Figure 15) is attributed to closure of pores and cracks [*Birch*, 1960; *Rey et al.*, 1994]. Delayed reopening of cracks during depressurization induced hysteresis with apparent higher velocities than during pressurization at the same confining pressure. For both the protolith and the mylonite, quasi-linear curves at confining pressure higher than 250 MPa indicate that intrinsic properties of the samples are approached. Intrinsic properties of the gradient zone were not reached at 300 MPa. At this confining pressure, average *P* wave velocities are mini-

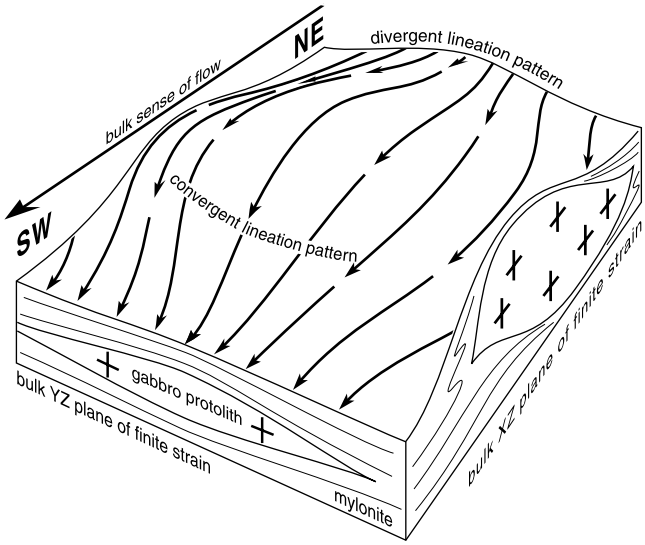

Figure 20. Block diagram sketching divergent and convergent lineation patterns in mylonite around a protolith lens.

mum in the protolith (V_p = 7.090 km s^{-1}) and maximum in the mylonite (V_p = 7.202 km s^{-1}; Table in Figure 15). The measured V_p = 7.135 km s^{-1} in the gradient samples is consistent with an average of V_p = 7.146 km s^{-1} calculated from velocities in the two previous zones, if we assume that *P* wave velocity and anisotropy evolve gradually from protolith to mylonite. Increasing *P* wave velocities are correlated with density increase: 2.997 kg m^{-3} for the protolith and 3.081 kg m^{-3} for the mylonite. The highest density of the pargasite-garnet-bearing mylonite points to increased pressure conditions from crystallization of the gabbro to metamorphic recrystallization within the mylonite. The point is that a 2.8% increase in density does not explain the average 48% surface loss measured in the vorticity profile plane of the shear zone. We conclude that out-of-plane material motion and not volume loss is responsible for departure from ideal simple shear, an interpretation also preferred by *Srivastava et al.* [1995] and *Bhattacharyya and Hudleston* [2001].

5.3. Three-Dimensional Shape-Preferred Orientation (SPO) in Mylonites

[35] Image analysis of [*XZ*] planes cannot yield information on the 3-D geometry of the flow. The 3-D measurements of the SPO (Figure 16) were made on [*XZ*], [*YZ*], and [*XY*] polished sections observed in Scanning Electron Microscopy (SEM) and analyzed with the intercept method. The 3-D fabric is calculated from the three orthogonal roses of directions using a quadratic shape tensor construction [*Robin*, 2002]. The shape fabrics of pargasite and plagioclase are axial symmetric, with short axes nearly orthogonal to the foliation (Figure 16), which suggests flattening during shape acquisition. Because pargasite is synkinematic the corresponding strain ratio is weak. The predeformation plagioclase has SPOs that record more of the deformation; they plot in the flattening field of the Flinn diagram (Figure 17), which gives further evidence for nonideal simple shear in mylonites. Quartz yielded scattered ellipse directions (Figure 16) that do not provide information on the strain regime because strain ratios indicate nearly spherical shape (Figure 17).

5.4. Three-Dimensional Lattice-Preferred Orientation (LPO) of Mylonite Amphiboles

[36] The LPO of pargasitic amphibole was measured on a polished [*XZ*] section of the ASZ 1 mylonite using SEM-based electron backscatter diffraction (EBSD) technique [*Venables and Harland*, 1973]. Amphibole was chosen because it represents a single crystallization event characteristic of the mylonite assemblage, whereas quartz and feldspar possibly comprise new grains along with clasts of the magmatic assemblage.

[37] The pargasite LPO displays a well-defined girdle of *c*[001] axes close to the [*XY*] foliation plane with a maximum, making an angle of less than 10° to the stretching direction *X* (Figure 18). The pole figure of *a*[100] axes displays maximum concentrations normal to the *c*[001] girdle, while *b*[010] poles are poorly oriented. Pargasite thus has an axial symmetric LPO that is superposed to its SPO, which does not comply with ideal simple shear geometry of flow. As discussed for the plagioclase SPO, these fabric characteristics suggest mylonite flow out of the [*XZ*] plane.

6. Discussion and Field Evidence

[38] Structural observations from excellent 3-D outcrops confirm sideways displacement of mylonitic material around lenses of less deformed gabbro. Folded mylonite between adjacent lenses (Figures 19a and 19b), folds (ASZ 1, Figure 3), and local variations in the direction of the stretching lineation mark changes in flow geometry around stiff lenses [*Hudleston*, 1999]. Systematic structural measurements and particularly well-exposed examples allow identifying two types of out-of-[*XZ*]-plane flow that occur within the same shear zone but at different sites with respect to the surrounded protolith lens.

[39] All shear zones have a ''thinning'' component. Mylonites are widening (*Y* or *b* axis elongation in finite strain or kinematic reference frames, respectively; transpression shear zone models of *Sanderson and Marchini* [1984], the ef-X_I monoclinic shear zones of *Passchier* [1998] with e and f representing the eigenvectors parallel to the shear zone boundaries) on the ''back'' (facing the flow) of lenses. A divergent lineation pattern gives evidence for widening mylonitic flow (Figure 20). Mylonites are narrowing, hence lengthening (*X* or *a* axis elongation in finite strain or kinematic reference frames, respectively; stretching shear zone models of *Means* [1989], the ef-Y_I monoclinic shear zones of *Passchier* [1998]) in ''front'' (lee) of lenses. A convergent lineation pattern gives evidence for lengthening mylonitic flow (Figure 20). Flow changes are spatially progressive and also depend on local accommodation between neighboring lenses. Lengthening mylonites also occur between boudins of a former lens that has been split by anastomosing shear zones (Figures 19a and 19b), the mylonite being apparently sucked in between separating boudins. Widening mylonites are identified in [*YZ*] sections (Figures 19c and 19d). Passive markers such as hornblendite or felsic veins, along with changes in the

direction of the mineral lineation, reveal the sideways departure from simple shear flow. Convergent and divergent lineation patterns explain the wide distribution of lineation measurements with strong widening shear zones representing 20% of the 150 measured ones (Figure 1b).

[40] The measured strain gradients and field observations shed some light on mechanisms that governed strain localization during the emplacement of gabbros in the lowest crust of the Kohistan Arc. Hypotheses concerning strain localization in sheared homogeneous rocks are often based on grain-size models [*Dutruge et al.*, 1993], whereas in heterogeneous rocks, initial weaknesses like compositional contacts, minerals with different rheology, and/or fluid-rich zones are expected to favor localization by strain-weakening processes [e.g., *Sørensen*, 1983; *Dutruge and Burg*, 1997; *Rutter*, 1999; *Goodwin and Tikoff*, 2002]. ASZ 57 shows that in the studied bimineralic gabbro, shear zones tend to develop along the borders of plagioclase-rich patch-like domains (Figures 5 and 6), which make the only discernible heterogeneities. Accordingly, the relative proportion of the weakest mineral governed strain localization. Lengthwise propagation and coalescence of the shear zones resulted in the anastomosing pattern whose geometry portrays the bulk shear regional deformation [*Arbaret et al.*, 2000].

7. Conclusions

[41] Strain analysis, crystallographic and shape fabrics, geochemical, and seismic properties of the shear zones developed in a gabbro of the Kohistan paleo-island arc show that deep crustal anastomosing patterns reflect complex flow overlooked in most previous work. In particular, they are as follows:

[42] 1. Passive deformation of the magmatic assemblage produced short shear zones bordering weakest, plagioclase-rich domains during the late magmatic emplacement of the gabbros. The distribution of the weakest mineral phase is therefore a key parameter of shear strain localization in a rather homogeneous rock.

[43] 2. Lengthwise propagation and coalescence of discrete shear zones during subsequent solid-state deformation resulted in the pervasive asymmetric pattern of shear zones. In Kohistan this evolution took place under prograde and isochemical amphibolite, subgranulite facies metamorphism.

[44] 3. Two subzones are distinguished in strain gradients. In low-strain and external domains, deformation is simple shear of the crystalline aggregate. In high-strain and mylonite domains, grain-size reduction, recrystallization of pargasite and quartz, and new growth of OH-bearing phases accommodate thinning components of the flow.

[45] 4. Lengthwise variations of flow produce widening and lengthening shear zones on rear and lee flanks of protolith lenses, respectively.

[46] 5. Changes in flow types are revealed from strain, SPO, and LPO measurements in the three spatial dimensions. The 2-D strain analysis commonly applied to vorticity profile planes of shear zones provides no information on the out-of-[*XZ*]-plane shear flow.

[47] **Acknowledgments.** The Swiss National Science Foundation (grant 20-49372.96) has supported this work. We thank L. Burlini for precious assistance in seismic property measurement and K. Kunze for his incomparable expertise in EBSD techniques. Generous help from N. Chaudhry, S. Hussain, and H. Dawood for field logistics was also essential. C. Talbot and B. Tikoff made detailed and extremely pertinent reviews that helped us to clarify descriptions and concepts.

References

Arbaret, L., J. P. Burg, G. Zeilinger, N. Chaudhry, S. Hussain, and H. Dawood, Pre-collisional anastomosing shear zones in the Kohistan Complex (NW Pakistan), in *Tectonics of Western Himalaya and Karakoram*, edited by M. A. Khan et al., *Geol. Soc. Spec. Publ.*, *170*, 295–311, 2000.

Bard, J. P., Metamorphism of an obducted island arc: Example of the Kohistan sequence (Pakistan) in the Himalayan collided range, *Earth Planet. Sci. Lett.*, *65*, 133–144, 1983.

Berthé, D., P. Choukroune, and P. Jégouzo, Orthogneiss, mylonite and non-coaxial deformation of granite: The example of the South Armorican Shear Zone, *J. Struct. Geol.*, *1*, 31–42, 1979.

Bhattacharyya, P., and P. Hudleston, Strain in ductile shear zones in the Caledonides of northern Sweden: A three-dimensional puzzle, *J. Struct. Geol.*, *23*, 1549–1565, 2001.

Birch, F., The velocity of compressional waves in rocks to 10 kilobars, part 1, *J. Geophys. Res.*, *65*, 1083–1102, 1960.

Burg, J.-P., and P. Laurent, Strain analysis of a shear zone in a granodiorite, *Tectonophysics*, *47*, 15–42, 1978.

Burg, J.-P., J.-L. Bodinier, S. Chaudhry, S. Hussain, and H. Dawood, Infra-arc mantle-crust transition and intra-arc mantle diapirs in the Kohistan Complex (Pakistani Himalaya): Petrostructural evidence, *Terra Nova*, *10*, 74–80, 1998.

Coward, M. P., R. D. Broughton, I. W. Luff, M. G. Petterson, C. J. Pudsey, D. C. Rex, and M. A. Khan, Collision tectonics in the NW Himalayas, in *Collision Tectonics*, edited by M. P. Coward and A. C. Ries, pp. 203–219, Blackwell Sci., Malden, Mass., 1986.

Dutruge, G., and J.-P. Burg, Strain localization in an orthogneiss laccolith (the Pinet Massif, Aveyron, southern France), *Tectonophysics*, *280*, 47–60, 1997.

Dutruge, G., J. Chéry, and J. E. Hurtrez, Une approche numérique des effets de la taille de grain sur la localisation de la déformation, *C. R. Acad. Sci., Ser. II*, *317*, 195–201, 1993.

Dutruge, G., J.-P. Burg, and J. Lapierre, Shear strain analysis and periodicity within shear gradients of metagranite shear zones, *J. Struct. Geol.*, *17*, 819–830, 1995.

Escher, A., J. C. Escher, and J. Watterson, Reorientation of the Kangâmiut Dyke Swarm, West Greenland, *Can. J. Earth Sci.*, *12*, 158–173, 1975.

Flinn, D., On the symmetry principle and the deformation ellipsoid, *Geol. Mag.*, *102*, 36–45, 1965.

Gapais, D., P. Bale, P. Choukroune, P. R. Cobbold, Y. Mahjoud, and D. Marquer, Bulk kinematics from shear zone patterns: Some field examples, *J. Struct. Geol.*, *9*, 635–646, 1987.

Glazner, A. F., and J. M. Bartley, Volume loss, fluid flow and state of strain in extensional mylonites from the central Mojave Desert, California, *J. Struct. Geol.*, *13*, 587–594, 1991.

Goodwin, L. B., and B. Tikoff, Competency contrast, kinematics, and the development of foliations and lineations in the crust, *J. Struct. Geol.*, *24*, 1065–1085, 2002.

Grant, J. A., The isocon diagram—A simple solution to Gresens' equation for metasomatic alteration, *Econ. Geol.*, *81*, 1976–1982, 1986.

Gresens, R. L., Composition-volume relationships for metasomatism, *Chem. Geol.*, *2*, 47–55, 1967.

Hudleston, P., Strain compatibility and shear zones: Is there a problem?, *J. Struct. Geol.*, *21*, 923–932, 1999.

Launeau, P., and P.-Y. F. Robin, Fabric analysis using the intercept method, *Tectonophysics*, *267*, 91–119, 1996.

Launeau, P., J. L. Bouchez, and K. Benn, Shape preferred orientation of object populations: Automatic analysis of digitized images, *Tectonophysics*, *180*, 201–211, 1990.

March, A., Mathematische Theorie der Regelung nach der Korngestalt bei affiner Deformation, *Z. Kristallogr. Kristallgeom. Kristallphys.*, *81*, 285–297, 1932.

Mauler, A., L. Burlini, K. Kunze, P. Philippot, and J.-P. Burg, *P* wave anisotropy in eclogites and relationship to the Omphacite crystallographic fabric, *Phys. Chem. Earth, Part A*, *25*, 119–126, 2000.

Means, W. D., Stretching faults, *Geology*, *17*, 893–896, 1989.

Means, W. D., Shear zones and rock history, *Tectonophysics*, *247*, 157–160, 1995.

Michibayashi, K., S. Togami, M. Takano, M. Kumazawa, and T. Kageyama, Application of scanning X-ray analytical microscope to the petrographic characterization of a ductile shear zone: An alternative method to image microstructures, *Tectonophysics*, *310*, 55–67, 1999.

Newman, J., and G. Mitra, Lateral variations in mylonite zone thickness as influenced by fluid-rock interactions, Linville Falls fault, North Carolina, *J. Struct. Geol.*, *15*, 849–863, 1993.

O'Hara, K. D., Fluid flow and volume loss during mylonitization: An origin for phyllonite in an overthrust setting, North Carolina, U.S.A., *Tectonophysics*, *156*, 21–36, 1988.

O'Hara, K. D., Fluid-rock interaction in crustal shear zones: A directed percolation approach, *Geology*, *22*, 843–846, 1994.

Passchier, C. W., Monoclinic model shear zones, *J. Struct. Geol.*, *20*, 1121–1137, 1998.

Ramsay, J. G., Shear geometry: A review, *J. Struct. Geol.*, *2*, 83–99, 1980.

Ramsay, J. G., and I. Allison, Structural analysis of shear zones in a Alpinised Hercynian Granite (Maggia Lappen, Pennine Zone, central Alps), *Schweiz. Mineral. Petrogr. Mitt.*, *59*, 251–279, 1979.

Ramsay, J. G., and R. H. Graham, Strain variation in shear belts, *Can. J. Earth Sci.*, *7*, 786–813, 1970.

Rey, P. F., D. M. Fountain, and W. P. Clement, *P* wave velocity across a noncoaxial ductile shear zone and its associated strain gradient: Consequences for upper crustal reflectivity, *J. Geophys. Res.*, *99*, 4533–4548, 1994.

Riedel, W., Zur Mechanik geologischer Bruchersheinungen, *Zentralblatt Miner. Geol. Palaeontol., Abt. B*, *29*, 354–368, 1929.

Ring, U., Volume loss, fluid flow, and coaxial versus noncoaxial deformation in retrograde, amphibolite facies shear zones, northern Malawi, east-central Africa, *Geol. Soc. Am. Bull.*, *111*, 123–142, 1999.

Robin, P. Y. F., Determination of fabric and strain ellipsoids from measured sectional ellipses: Theory, *J. Struct. Geol.*, *24*, 531–544, 2002.

Robin, P. Y. F., and A. R. Cruden, Strain and vorticity patterns in ideally ductile transpression zones, *J. Struct. Geol.*, *16*, 447–466, 1994.

Rutter, E. H., On the relationship between the formation of shear zones and the form of the flow law for rocks undergoing dynamic recrystallization, *Tectonophysics*, *303*, 147–158, 1999.

Saltikov, S. A., *Stereometric Metallography*, 2nd ed., Metallurgizdat, Moscow, 1958.

Sanderson, D. J., and R. D. Marchini, Transpression, *J. Struct. Geol*, *6*, 449–549, 1984.

Schaltegger, U., G. Zeilinger, M. Frank, and J.-P. Burg, Multiple mantle sources during island arc magmatism: U-Pb and Hf isotopic evidence from the Kohistan arc complex, Pakistan, *Terra Nova*, *14*, 1–8, 2002.

Sørensen, K., Growth and dynamics of the Nordre Strøm-fjord shear zone, *J. Geophys. Res.*, *88*, 3419–3437, 1983.

Srivastava, H. B., P. Hudleston, and D. Earley, Strain and possible volume loss in a high-grade ductile shear zone, *J. Struct. Geol.*, *17*, 1217–1231, 1995.

Tahirkheli, R. A. K., M. Mattauer, F. Proust, and P. Tapponnier, The India Eurasia suture zone in northern Pakistan: Synthesis and interpretation of recent data at plate scale, in *Geodynamics of Pakistan*, edited by A. Farah and K. A. DeJong, pp. 125–130, Geol. Surv. of Pakistan, Quetta, 1979.

Tchalenko, J. S., The evolution of kink bands and the development of compression textures in sheared clays, *Tectonophysics*, *6*, 159–174, 1968.

Tikoff, B., and H. Fossen, Simultaneous pure and simple sear: The unifying deformation matrix, *Tectonophysics*, *217*, 267–283, 1993.

Treloar, P. J., D. C. Rex, P. G. Guise, M. P. Coward, M. P. Searle, B. F. Windley, M. G. Petterson, M. Q. Jan, and I. W. Luff, K-Ar and Ar-Ar geochronology of the Himalayan collision in NW Pakistan: Constraints on the timing of suturing, deformation, metamorphism and uplift, *Tectonics*, *8*, 881–909, 1989.

Treloar, P. J., K. H. Brodie, M. P. Coward, M. Q. Jan, M. A. Khan, R. J. Knipe, D. C. Rex, and M. P. William, The evolution of the Kamila shear zone, Kohistan, Pakistan, in *Exposed Cross-Sections of the Continental Crust*, edited by M. H. Salisbury and D. M. Fountain, pp. 175–214, Kluwer Acad., Norwell, Mass., 1990.

Treloar, P. J., M. G. Petterson, M. Q. Jan, and M. A. Sullivan, A re-evaluation of the stratigraphy and evolution of the Kohistan arc sequence, Pakistan Himalaya: Implications for magmatic and tectonic arc-building processes, *J. Geol. Soc. London*, *153*, 681–693, 1996.

Venables, J. A., and C. J. Harland, Electron back-scattering patterns—A new technique for obtaining crystallographic information in the scanning electron microscope, *Philos. Mag.*, *27*, 1193–1200, 1973.

Yoshino, T., H. Yamamoto, T. Okudaire, and M. Toriumi, Crustal thickening of the lower crust of the Kohistan arc (N. Pakistan) deduced from Al zoning in clinopyroxene and plagioclase, *J. Metamorph. Geol.*, *16*, 729–748, 1998.

Zeilinger, G., Structural and geochronological study of the lowest Kohistan complex, Indus Kohistan region in Pakistan, NW Himalaya, doctoral dissertation, 243 pp., Naturwiss. ETH Zürich, Zürich, 2002.

L. Arbaret, Institut des Sciences de la Terre, UMR 6113, CNRS, Université d'Orléans, 1A, Rue de la Férollerie, F-45071, Orléans Cédex 2, France. (laurent.arbaret@univ-orleans.fr)

J.-P. Burg, Geologisches Institut, ETH-Zentrum, Sonnegstrasse 5, CH-8092, Zürich, Switzerland.